ADVANCED ELECTRONIC MATERIALS
www.advelectronicmat.de

Characterization of Aerosol Deposited Cesium Lead Tribromide Perovskite Films on Interdigited ITO Electrodes

Albert These, Neamul H. Khansur, Osbel Almora, Larry Luer, Gebhard J. Matt, Udo Eckstein, Anastasia Barabash, Andres Osvet, Kyle G. Webber, and Christoph J. Brabec*

Aerosol deposition (AD) is a promising additive manufacturing method to fabricate low-cost, scalable films at room temperature, but has not been considered for semiconductor processing, so far. The successful preparation of cesium lead tribromide ($CsPbBr_3$) perovskite films on interdigitated indium tin oxide (ITO) electrodes by means of AD is reported here. The 20–35 µm thick layers are dense and have good adhesion to the substrate. The orthorhombic *Pnma* crystal structure of the precursor powder was retained during the deposition process with no signs of defect formation. The formation of electronic defects by photoluminescence spectroscopy is investigated and found slightly increased carrier recombination from defect sites for AD films compared to the powder. A nonuniform defect distribution across the layer, presumably induced by the impact of the semiconducting grains on the hard substrate surface, is revealed. The opto-electronic properties of AD processed semiconducting films is further tested by electrical measurements and confirmed good semiconducting properties and high responsivity for the films. These results demonstrate that AD processing of metal halide perovskites is possible for opto-electronic device manufacturing on 3D surfaces. It is believed that this work paves the way for the fabrication of previously unimaginable opto-electronic devices by additive manufacturing.

1. Introduction

Aerosol deposition method (AD) is a room temperature deposition technique that utilizes the high kinetic energy of ejected aerosol consisting of a mixture of submicrometer-sized dry ceramic particles and carrier gas, e.g., N_2, He, O_2, or air, from a specially designed nozzle. Room temperature deposition of the dense and mechanically stable ceramic films is not possible with conventional film deposition methods requiring high temperature (> 500 °C) densification. Therefore, AD has a unique advantage of the convenient integration of dense ceramic layers with temperature-sensitive substrates or electrodes. Additionally, the AD process is a rapid and cost-effective method for large-scale production of ceramic films due to the fast deposition rate. As such, AD has been implemented for the industrial manufacturing of thick films/coating in different areas, such as microelectronics, wear-resistance coatings, biomedical implants, solid-oxide fuel cells, gas sensors, and humidity sensors.[1] However, processing of optoelectronic perovskite semiconducting devices was not yet reported to our knowledge.

The AD process is a promising method for the fabrication of perovskite halides, given that the film/layer quality does not directly depend on the synthesis procedure of the perovskite phase. Several research works have shown the feasibility of AD layer processing in the field of dye-sensitized solar cells[2] as well as hybrid halide perovskites.[3] For example, the photoluminescence (PL) spectrum of

A. These, Dr. O. Almora, Dr. L. Luer, Dr. G. J. Matt, Dr. A. Barabash, Dr. A. Osvet, Prof. C. J. Brabec
Friedrich-Alexander-University Erlangen-Nuremberg
Department of Materials Science and Engineering
Institute of Materials for Electronics and Energy Technology (i-MEET)
Martensstrasse 7, Erlangen 91058, Germany
E-mail: albert.these@fau.de

The ORCID identification number(s) for the author(s) of this article can be found under https://doi.org/10.1002/aelm.202001165.

DOI: 10.1002/aelm.202001165

A. These, Dr. O. Almora
Friedrich-Alexander-University Erlangen-Nuremberg
Erlangen Graduate School in Advanced Optical Technologies (SAOT)
Paul-Gordan-Strasse 6, Erlangen 91052, Germany
Dr. N. H. Khansur, U. Eckstein, Prof. K. G. Webber
Friedrich-Alexander-University Erlangen-Nuremberg
Department of Materials Science and Engineering
Institute of Glass and Ceramics
Martensstrasse 5, Erlangen 91058, Germany
Dr. O. Almora
Universitat Jaume I
Institute of Advanced Materials (INAM)
Castellón de la Plana, Castellón 12006, Spain

the AD-processed $CH_3NH_3PbI_3$ showed typical optical features that are consistent with films prepared with other methods.[3] AD has also been used to fabricate inorganic halide perovskite coated oxide ceramic films, such as, $CsPbBr_3/Al_2O_3$, $CsPb_2Br_5/BaTiO_3$, and $CsPbBr_3/TiO_2$, for application as humidity sensors.[4] In these cases, authors used a chemical route to create core–shell type particles of oxide ceramics, where the halide perovskite was the shell. However, no report on the fabrication of optoelectronic semiconducting devices is available. Here, we demonstrate AD deposited CsPbBr3 layers on interdigitated electrodes and explore their electronic but also optoelectronic properties. Previous studies have shown that the AD processing, i.e., the unique dynamic deposition process frequently influences the electrical properties of AD deposited functional dielectric ceramics layers. This necessitates an in-depth investigation on the defect formation of our CsPbBr3 deposited films. A combination of X-ray, time resolved photoluminescence spectroscopy (TRPL), impedance, electrical and optoelectronic measurements were performed to precisely identify the formation of structural or electronic defects as a function of AD processing.

We therefore demonstrate the feasibility of processing a halide perovskite for optoelectronic application by means of AD fabrication. The influence of AD processing on the photophysical and electric properties $CsPbBr_3$ is elucidated in-depth for the first time and the characterizations revealed that the semiconducting properties are maintained. The $CsPbBr_3$ films are only slightly affected by the AD process, due to the high defect tolerance of metal halide perovskites. High responsivity, a remarkable stability and the possibility to fabricate unusual device geometries pave the way for previously unimaginable optoelectronic devices.

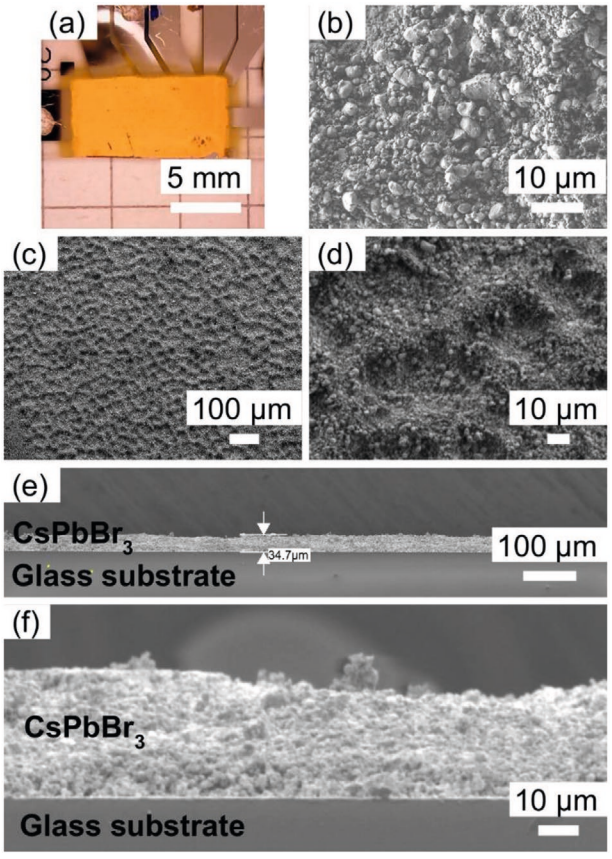

Figure 1. a) Overview photograph of the as-deposited $CsPbBr_3$ film on an ITO/glass substrate. Scanning electron microscope images depicting: b) individual particles with heterogenous particle size distribution c) rough surface morphology d) craters that cover the whole film. e) Cross sectional image revealing a layer thickness of 34.7 µm. f) Layer has excellent contact to the substrate without delamination.

2. Results and Discussion

2.1. Microstructural and Structural Characterization

An overview photograph and micrograph images of the AD film morphology is shown in **Figure 1**. A cohesive $CsPbBr_3$ perovskite layer was successfully formed at room temperature on an interdigitated indium tin oxide (ITO) substrate (Figure 1a). The layer formation did not include sintering, as the individual powder grains are still visible under higher magnification (Figure 1b). Particle sizes are widely spread and range from few hundreds of nanometers to about 10 μm, similar to the powder. The surface is homogenous and dense. We observed only a few defect gaps that are not covered by the powder, as seen in the overview image. According Figure 1c,d, the surface morphology is rough and completely covered with craters. They are most likely caused by the impact collision of big particles during the deposition process.[5]

Cross-sectional images in Figure 1e reveal a film thickness of about 35 µm with only minor variations due to the craters. The as-deposited film has direct contact with the substrate and forms a mechanically stable substrate-film interface without any apparent interfacial delamination and, although scratch or adhesion testing was not performed, no edge or buckle delamination was observed following deposition or during subsequent handling, processing, or measurement of the film (Figure 1f).

The X-ray diffraction patterns for both the as-processed $CsPbBr_3$ powder and AD processed film are presented in **Figure 2**. The results show no sign of secondary phases within the detection limit of the instrument used. Full-pattern structural refinement (Figure 2a) shows orthorhombic crystal structure with *Pnma* (a = 8.2550(3) Å, b = 11.7584(4) Å, c = 8.2077(4) Å, and V = 796.6955 Å3) space group. The structural parameters are consistent with those previously reported.[6] The crystal structure of the AD film did not show any significant change due to the dynamic deposition process. However, the structural parameters were found to be slightly different (a = 8.2515(4) Å, b = 11.7529(4) Å, and c = 8.2037(3) Å, and V = 795.5901 Å^3) to those of the powder sample, i.e., the unit cell volume of $CsPbBr_3$ in the AD processed film is smaller than the as-processed powder. This is possibly related to the compressive residual stresses induced by the AD process.[7] It should be mentioned here that generally, the as-processed AD films exhibit significantly broadened peaks as compared to the corresponding powder samples. This is argued to be due to the crystallite size and/or microstrain broadening associated with the dynamic loading process of the AD. However, in the case of $CsPbBr_3$, no significant change was observed in the peak width. The origin of such behavior is possibly related to the mechanical properties of the $CsPbBr_3$.[8] For instance, Young's modulus

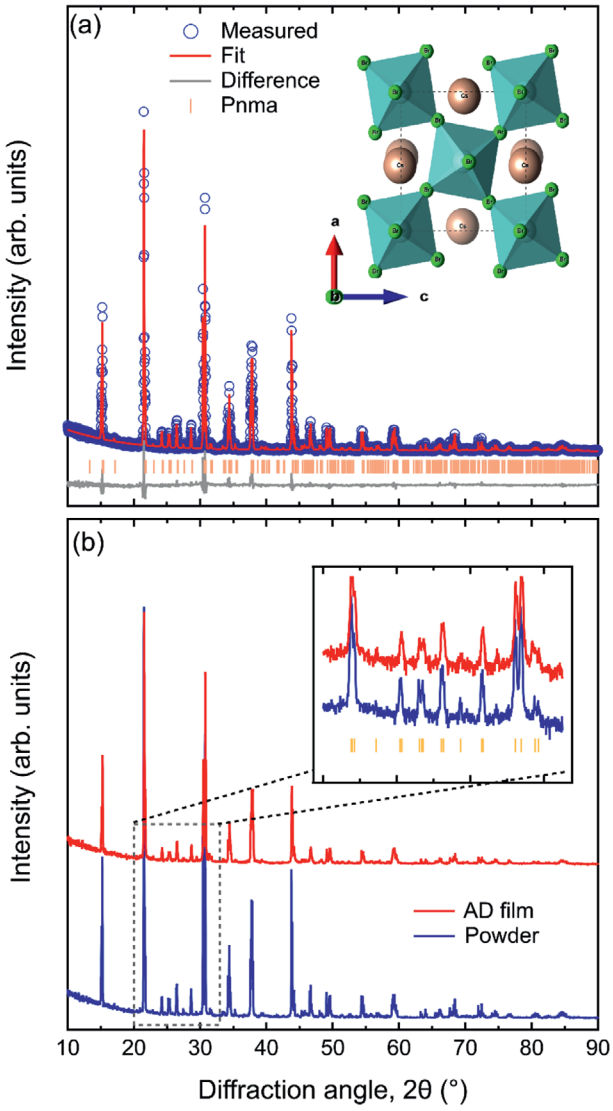

Figure 2. a) The Rietveld refinement results of X-ray diffraction patterns for the as-processed powder. b) X-ray diffraction pattern of the AD processed film and the powder. The inset of (a) and (b) shows the Pnma unit cell with octahedra tilting and the enlarged 20°–33° 2θ region, respectively.

of single-crystalline <101> $CsPbBr_3$ has been reported to be 15.8 GPa which is approximately an order of magnitude lower than oxide perovskite single crystal such as $BaTiO_3$ (128 GPa).[9] It is suggested that the $CsPbBr_3$ particles displayed an increased plastic deformation during AD processing in comparison to brittle ceramics. Although this effect was not quantified and is an important area for future research, it was observed that $CsPbBr_3$ particles deformed more like soft metallic particles than brittle ceramic particles. The higher plastic deformation could act to relax the AD process-induced stress without fracturing the particle significantly. Therefore, the AD process-induced crystallite size and/or microstrain broadening in the case of $CsPbBr_3$ is expected to be lower. Nevertheless, the diffraction results highlight that the AD deposition process does not detrimentally affect the crystal structure of the $CsPbBr_3$. The results of the structural and microstructural characterization clearly show that the AD process is a feasible technique to fabricate compact layers of $CsPbBr_3$ at room temperature.

2.2. Optical Characterization

The rather harsh deposition conditions deployed for our AD films raise the question whether the photophysics of the perovskite materials is still preserved. Normalized absorbance spectra for the crystalline $CsPbBr_3$ powder and AD film are depicted **Figure 3**a. The AD films were either illuminated from the top side of the AD film (frontside) or through the glass substrate (backside). Note than the deviation at low wavelengths below 500 nm for the backside plot stems from the illumination through the glass substrate. Both the powder and AD film show a clear absorption onset below 550 nm, typical for $CsPbBr_3$. Hereby, the absorption onset is slightly blue shifted for the AD films indicating a higher bandgap. A Tauc plot derived from the absorbance is shown in Figure S2 (Supporting Information) and reveals a bandgap of ≈2.28 eV for the powder and ≈2.31 eV for the AD film, comparable to previously reported values.[6,10] This bandgap increase for the AD film can be explained with the abovementioned reduction in unit cell size after AD processing.

Time-integrated PL spectra of the AD films and the microcrystalline powder were recorded at room temperature and are shown in Figure 3b. The PL spectra reveal two peaks for

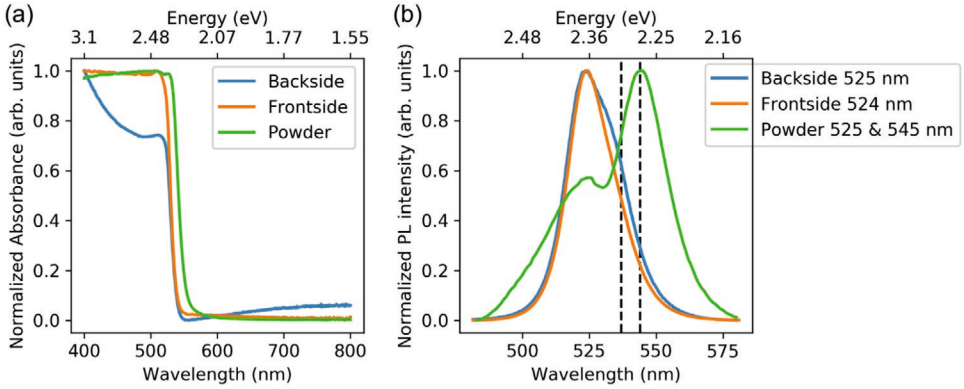

Figure 3. Wavelength scale is correct, energy scale is shown for convenience. a) Normalized absorbance of the $CsPbBr_3$ powder and AD processed film. b) Normalized PL spectra of $CsPbBr_3$ powder AD films under 402.5 nm excitation. The legend states the PL peak wavelengths. The two black dashed lines represent the bandgap energy of 2.28 and 2.31 eV for the powder and AD film, respectively.

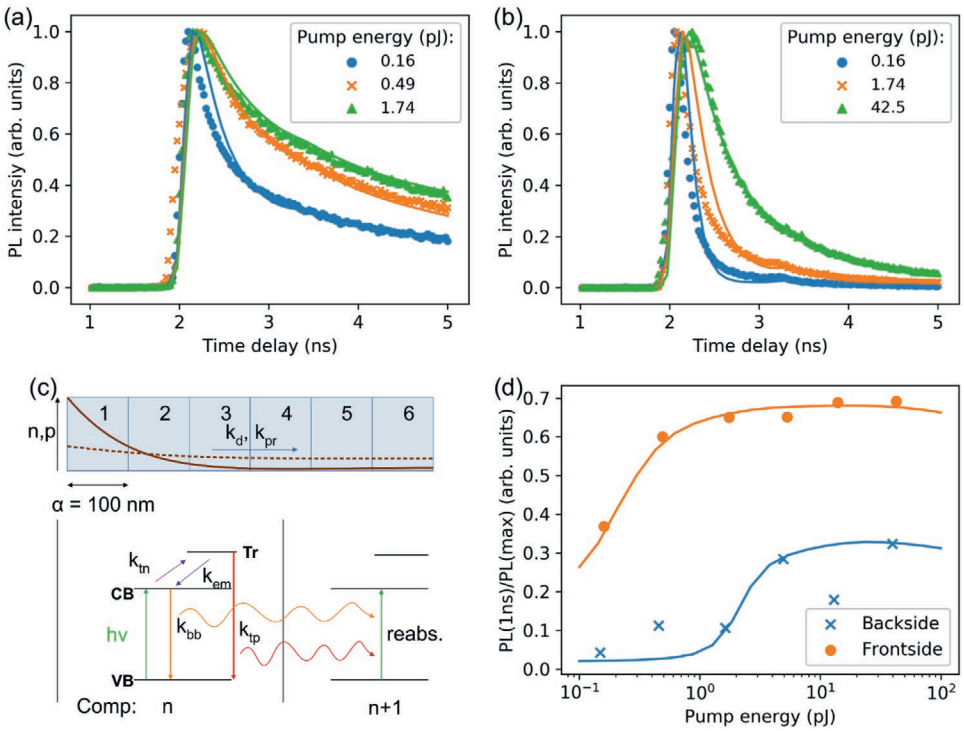

Figure 4. a,b) TRPL in AD films, after illumination from the a) frontside and b) backside and detected at the peak wavelength at different pulse intensities, as given in the inset (symbols). Curves of same color as symbols are the corresponding global fits according to a numerical rate equation model as shown in (c). To correctly account for photon recycling and carrier diffusion, 6 compartments were calculated. In the lower part of (c), processes occurring in a single compartment are depicted. In the upper part of (c), intercompartmental processes are given. Initially, the photoinduced carrier distribution follows the Beer–Lambert law (brown solid line), while at a later stage, carrier diffusion into the nonilluminated depth of the sample will cause a dilution effect reducing radiative recombination (dashed brown curve). d) Intensity dependence of the dynamics of the initial decay, given as the ratio PL(t = 1 ns)/PL(max) (symbols). The curves give the prediction by the global fits using the best fitting parameters from Table 1.

the powder with a local maximum at 525 nm and a global maximum at 545 nm. Both peaks stem from the recombination of bound excitons.[6] The emission at 545 nm fits very well to band-to-band emission with a bandgap of 2.28 eV, which is indicated with a dashed black line.

The 525 nm peak can be attributed to electrons trapped in degenerate Br vacancy defects with energy levels in the conduction band (CB) that recombine with holes in the valence band (VB).[10a] The location of this Br vacancy of 0.09 eV above the CB edge is in reasonable agreement with the reported literature value of 0.16 eV.[11] The AD fabricated films are dominated by the Br vacancy band at 524/525 nm with a full width half at half maximum of 21/25 nm for the front- and backside, respectively. The band-to-band recombination peak is not visible in the spectrum, indicating a quenching of band-to-band recombination compared to the Br vacancy recombination at lower wavelengths.

We additionally performed TRPL experiments (**Figure 4**) of the AD films after frontside and backside illumination detected at the peak wavelengths of the samples (panels a and b, respectively) and fitted the resulting transients by a numerical model given in panel c. For both front- and backside illumination, we observe a very fast initial TRPL decay, active over the first nanoseconds, followed by a slower tail. The total dynamics of this fast initial decay is reduced at higher illumination intensity (as given in the insets in Figure 4a,b), which seems to indicate that the fast initial drop is related to a decay channel that can be saturated at higher illumination intensities. We highlight that a simple multiexponential model might have fit the data better than the numerical approach. However, we exploit the information provided by the intensity dependent dynamics by globally fitting all curves to a common set of parameters directly describing photophysical elementary processes. Such cannot be done by obtaining an unrelated list of exponential lifetimes for each intensity.

Comparing TRPL traces after front- and backside illumination at same intensities, it becomes evident that the TRPL decay is much faster after backside illumination than after frontside illumination. This holds for both the initial fast drop and the longer decay phase. Another important distinction between frontside and backside illumination is the illumination intensity level at which the TRPL traces become intensity independent. For frontside illumination, this occurs at intensities as low as 0.49 pJ, while for backside illumination, one order of magnitude higher intensities are needed to make the corresponding TRPL traces intensity independent. Thus, without any numerical modeling, we can conclude that the number of defects through which the fast initial decay takes place, is about one of order of magnitude higher close to backside than close to the frontside.

Overall, the TRPL decay in our AD films is fast compared to published results in thin film samples typically exhibiting

Table 1. Fitting parameters for the global fits shown in Figure 4a,b,d. Absolute uncertainties given in brackets. For details, see the Supporting Information. The parameter names refer to the processes given in Figure 4c.

Fit parameter	Front side illumination	Back side illumination
k_{bb} ($cm^3\ s^{-1}$)	$5(1) \times 10^{-10}$	$1.11(2) \times 10^{-8}$
k_{tn} ($cm^3\ s^{-1}$)	$5.7(9) \times 10^{-5}$	$9.5(4) \times 10^{-6}$
k_{em} ($cm^3\ s^{-1}$)	$2.8(2) \times 10^{-12}$	$9.2(2) \times 10^{-12}$
k_d (s^{-1})	$2.6(2) \times 10^{9}$	$<1 \times 10^{8}$
N_t (cm^{-3})	$9.5(3) \times 10^{13}$	$1.25(4) \times 10^{15}$

TRPL lifetimes in the 10 ns range.[12] This behavior can be attributed to two phenomena: i) in our experimental setup, we use very low photon densities (down to 1013 photoinduced electron–hole pairs per cm^3), allowing us to trace trapping kinetics in real time even though trap concentration is low, and ii) our films are much thicker than the typical light penetration depths in perovskites with a penetration depth (α) of about 100 nm.[13] Therefore, diffusion of photoinduced electron–hole pairs will be directed towards the nonilluminated depth of the sample thus causing a dilution effect causing a drop of TRPL. Also, photon recycling, caused by reabsorption of emitted photons, will statistically contribute to the build-up of a charge population in the depth of the sample, further accelerating the dilution effect causing the fast TRPL transient.

We globally fitted all TRPL traces to the numerical model given Figure 4c, explicitly taking into account the instrumental response function of the setup, and managed to reproduce all TRPL traces with the same set of fitting parameters with reasonable uncertainties (see **Table 1**). To account for the above mentioned dilution effects, we simulated the depth of the device by 6 compartments, each of a length corresponding to the light penetration depth α. Population transfer within each compartment is described by the scheme in the lower part of Figure 4c, while intercompartmental population transfer is considered by constants k_d and k_{pr}, referring to charge diffusion and photon recycling, respectively. In each compartment, we assume generation of electron–hole pairs by irradiation into the optically allowed band-to-band transition. Electrons in the CB can then either radiatively relax to the VB (constant k_{bb}), or become trapped in a neutral above-bandgap Br vacancy (constant k_{tn}). The charged Br vacancy becomes polaronic, thus inhibiting a re-emission of the electron into the CB.[10a] From a polaronic Br(-) vacancy, radiative recombination can occur with a hole from the VB. In order to keep the number of free parameters low, we neglect a possible direct generation of Br(-) vacancies by optical excitation (or by ultrafast transfer from higher energetic primary excitations), and we do not distinguish between radiative and nonradiative channels of Br(-) vacancy recombination.

The resulting global fits are given as solid curves in Figure 4a,b, and the corresponding fitting parameters are given in Table 1. The overall dynamics of all TRPL curves is well reproduced by the global fits, and the intensity dependence is rendered correctly. However, at very early times, some deviations between fit and experiment are visible; these might be due to experimental uncertainties or due to the limitations of the numerical model as indicated above. As shown in Table 1, the fitted values for the defect density are vastly different for frontside and backside illumination, thus confirming our qualitative notion.

In order to look into the intensity dependence in more detail, we simulated TRPL traces using the best fit constants from Table 1 for 20 different pulse energies in the experimentally covered range from 0.1 to 100 pJ. Figure 4d, we represent the TRPL intensity after 1 ns relative to the maximum value, PL(1ns)/PL(max), as a function of irradiation intensity (solid lines, with experimental points given as symbols). For front side illumination, the simulation is very well in line with the experiment, confirming the validity of the assumed model. For back side illumination, such a conclusion cannot be drawn, as the scatter of the experimental points is significant. On one hand, there is no doubt that the saturation of the light intensity dependence occurs at a much higher light intensity than after front side illumination (note the logarithmic horizontal axis); the fitted trap densities can therefore be considered as confirmed. On the other hand, the significant data scattering at higher illumination intensities makes it hard to predict at which level the saturation will occur; this gives some uncertainty to the fitted trap release rates. Furthermore, the simulated curves for both frontside and backside illumination predict a drop at very high light intensities which is not rendered by the experimental data points. In the Supporting Information, we show that this drop is caused by accelerated bimolecular band-to-band recombination, and that this happens if the photoinduced charges outnumber the majority holes introduced by the p-dopants. Assuming low acceptor concentrations A_n, this would happen at an even lower illumination intensity. We therefore fixed the acceptor concentration in our global fits to the value of 4.0×10^{17} cm^{-3}, for details see the Supporting Information.

Comparing the fitting constants for front side and back side illumination, we find that the rate of band-to-band recombination, k_{bb}, is one order of magnitude higher for back side illumination, a fact that is not easy to explain given the fact that this is an intrinsic material property and should not depend on the side of the illumination. We also find that the rate constant for trap filling, k_{tn}, is one order of magnitude lower after back side illumination. The trap filling rate constant is proportional to the trapping cross-section and the electron drift velocity; both are not expected to be so strongly different for frontside and backside illumination. We conjecture that this discrepancy can be explained by the introduction of an additional nonradiative trapping process occurring only close to the back side. Such additional traps could be caused by mechanical deformation of crystallites upon impact with the hard glass surface, distorting the band structure and introducing phonon-mediated decay channels. Moreover, these first layers on the bottom of the substrate are additionally fractured by the impact of subsequent collisions of powder particles increasing the defect density even further. This leads to a gradient of the defect density across the AD film thickness with the bottom layer having a higher defect density than the top layer.

Furthermore, the lower trap density for front side illumination can also be explained by defect passivation by molecular oxygen, forming superoxides, or by humidity.[14]

Additional mechanistic studies are under progress that will be published in a forthcoming specialized paper.

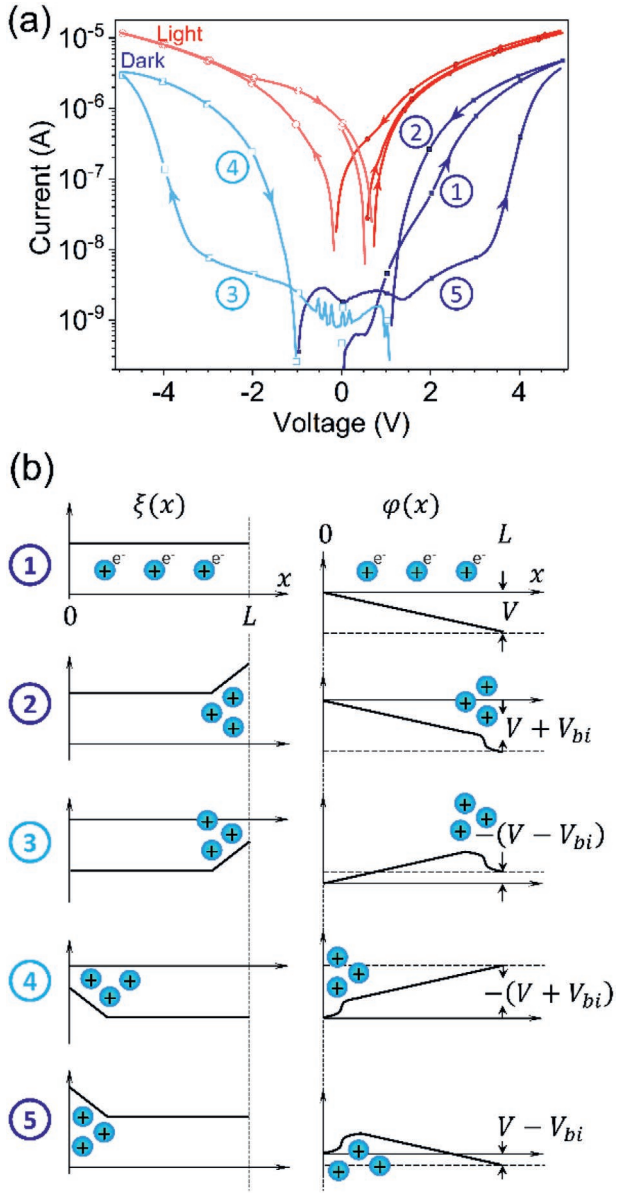

Figure 5. a) DC current–voltage characteristic of the 35 µm thick $CsPbBr_3$ sample in dark (squares-line) and under illumination (circles-line) at 100 mV s^{-1}. A significant photoconductivity increase is found under illumination, as well as hysteretic features which can be explained as due to space charges by drifted ions depending on the polarization routine. In (b) the electric field and electrostatic Galvani potential are depicted between electrodes at $x = 0$ and $x = L$ for the situations j–n in the dark curve of (a).

2.3. Electrical Characterization

The 35 µm thick sample was electrically characterized first in direct current (DC) mode by measuring the current–voltage ($I - V$) curve and then in alternating current (AC) mode by impedance spectroscopy (IS). The DC characteristic was sampled in dark and under illumination, as shown **Figure 5**a. First, a clear photoconductivity increase occurs under illumination as more than 10 times additional current was sensed for the $I - V$ after applied illumination intensity. A significant $I - V$ curve hysteresis of the sample is also observed in Figure 5a, even when it is symmetrically contacted. The drift of slow ions has characteristic times on the order of minutes, or even tens of minutes, which may form space charge regions toward the electrodes. This transient behavior can rectify currents on the order of µA during the time the potential barriers hold.

The effects on electric field ξ and electrostatic Galvani potential ϕ along a force line between the electrodes at $x = 0$ and $x = L$ is schemed in Figure 5b for each section of the external applied voltage sweep. For instance, during the bias sweep section j (0.0 to +5.0 V) in the dark $I - V$ of Figure 5a, the ions are still neutral and/or randomly distributed between the electrodes. But as bias is increased, and during the bias sweep section k (+5.0–0.0V), the drifted ions accumulate toward one electrode kinking the field and creating a built-in voltage V_{bi}. This situation is equivalent to an extra external applied voltage and, hence the current is lightly increased during k. Then, when the field is inverted in l (0.0 to −5.0 V) the V_{bi} created during k will hold for a while, rectifying currents in a sort of diode-like behavior. Afterward, the ions will drift again, but to the opposite electrode and in m (−5.0–0.0 V) the favorable V_{bi} increases the current, in a situation analogous to k. Likewise, the inversion of the field in n (0.0 to −5.0 V) rectifies the current once more, and subsequently we would go back to k, if the voltage is continuously swept. Interestingly, under illumination, the conductivity enhancement may overcome these transient built-in once the current exceeds a few µA.

The hysteresis-like drift of ions is also evident from the IS characterization, in Figure S3 (Supporting Information). There, the IS spectra are presented in several representations under light, at +5.0 V, and after 20 min of previous ±5.0 V. When the sample is held for sufficient time at +5.0 V the situation is similar to k in Figure 5b and the resistance comes from the smaller arc of the impedance Nyquist plot of Figure S3a (Supporting Information). Contrary, when the sample is measured at +5.0 V, but after 20 min of −5.0 V, the situation is similar to n in Figure 5b and the resistance comes from the largest arc of Figure S3a (Supporting Information) evolving in a sort of negative arc artifact as the situation k is again dominant. These artifacts are also evident in the negative capacitance of Figure S3b (Supporting Information) and "jumping" AC conductivity of Figure S3c (Supporting Information). Accordingly, IS measurements around equilibrium (0 V) are needed in order to discard the ion migration effects, and focus on the steady-state electrical properties.

At zero volts, the photoconductivity effect is also evident from the comparison between the IS spectra in dark and under illumination in the Nyquist plot of **Figure 6**a: more than 24 times higher resistance is found in dark than under illumination. In Figure 6a, two main arcs are evident, and from the experiment in Figure S3a (Supporting Information), both should comprise some amount of ionic contribution, which is a common feature in perovskites.[15] In the capacitance spectra of Figure 6b, it is evident that at least a third resistance-capacitance (RC) couple is present at the highest frequencies. Accordingly, in Figure 6a,b the experimental spectra (dots) were fitted (lines) to the equivalent circuit model in the inset of Figure 6b including at least three main RC couples. Fitting parameters and derived

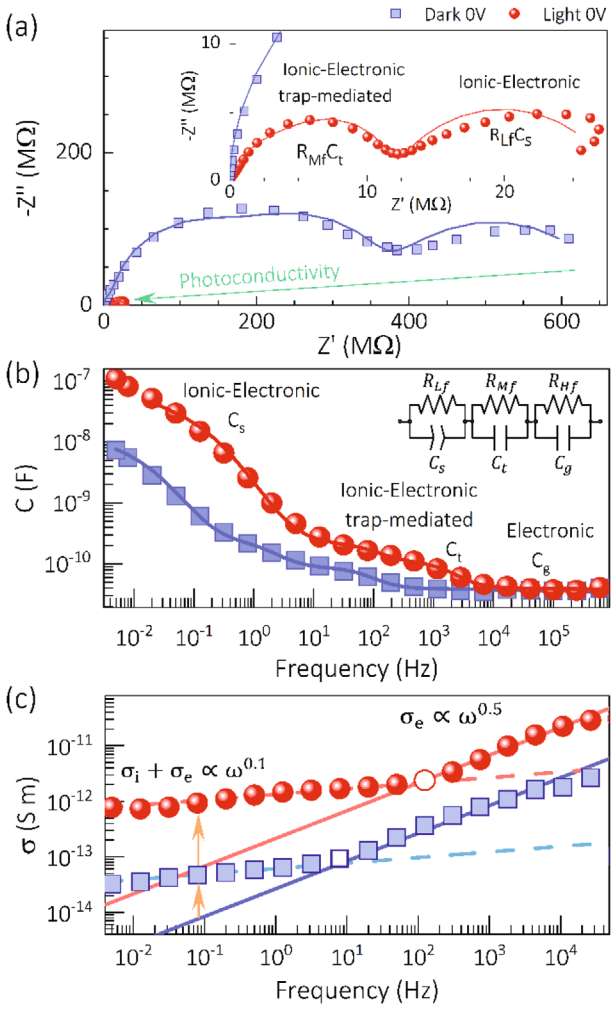

Figure 6. IS characterization of the 35 µm thick $CsPbBr_3$ sample at equilibrium in dark and under illumination in a) the impedance Nyquist plot representation and b) capacitance and c) AC conductivity Bode plot representations. Lines in (a) and (b) are the fittings to the equivalent circuit model inset in (b). Empty dots in (c) indicate ionic activation frequencies f_i.

characteristic times τ and AC conductivities σ are listed in Table S1 (Supporting Information).

At higher frequencies, above 10 kHz, a purely electronic process is dominant and a nearly light-independent capacitance plateau in Figure 6b indicates the geometrical capacitance C_g of the sample. This is coupled with the bulk electronic resistance R_{Hf} resulting in a characteristic time τ_e up to hundreds of microseconds. The corresponding electronic conductivity σ_e is in the order of µS. In the frequency range between 10 Hz and 1 kHz, the capacitance steps less than an order of magnitude possibly due to ionic-electronic and/or trap-mediated electronic capacitance C_t. The nature of C_t is also likely influenced by the overlapping effects of the ionic-electrode polarization type mechanisms observed at lower frequencies. For instance, in the biased experiment, the coupled resistance R_{Mf} in Figure S3a (Supporting Information) is sensitive to the ions drift artifacts, as C_t in Figure S3b (Supporting Information), but not in the same degree as the negative values at lower frequencies. The characteristic time τ_t for this process is up to hundreds of milliseconds and the conductivity σ_t is around units of nS. Note that the trap density associated with these middle-frequency features are most likely placed at the surface and grain boundaries.

At the lowest investigated frequencies, below 1 Hz, the most likely ionic-electronic electrode surface polarization capacitance C_s increases up to three orders of magnitude for the illuminated spectrum in Figure 6b. The coupling of C_s with the low-frequency resistance R_{Lf} is a typical feature in photovoltaic perovskites, commonly associated with interface phenomena in dark.[16] In the polarization experiment of Figure S3a,b (Supporting Information), one can see clear negative capacitance/impedance artifacts within the frequency range of this process. The characteristic time τ_i here is as high as tens of seconds and the conductivity σ_i is around units of nS.

Furthermore, the AC conductivity spectra report on interesting behavior, as presented in Figure 6c. Independently of the illumination or applied bias the electronic component of the conductivity follows the Jonscher's "universal" dielectric frequency response[17] which suggest a power law relation between the conductivity and the angular frequency $\sigma \propto \omega^s$. This feature is well-known in disordered solids[18] where several electronic conduction models[19] predict $0.5 \leq s \leq 1.0$ in ionic conducting glasses, and the diffusion-controlled relaxation model for ionic transport in glasses[20] predicts $0 < s < 0.5$. In Figure 6c equilibrium dark and under illumination spectra show two main regimes: at higher frequencies, a presumably more electronic conductivity behaves $\sigma_e \propto \omega^{0.5}$ and the extra contribution of ionic diffusion seems to rule the low frequency where $(\sigma_i + \sigma_e) \propto \omega^{0.1}$. The frequency ranges seem to agree with the earlier proposed physical meaning for the capacitive components in Figure 6b.

Note that the power s is not only characteristic of the material but the sample fabrication procedure, final morphology, and/or contact type. For instance, previous reports on AC conductivity from nanocrystalline $CsPbBr_3$ thin films[21] show s 0.7 – 1.0 at room temperature and s 0.3 above 400 K, while another study[22] showed power as high as s 1.7 from cubic shape $CsPbBr_3$ particles of up to 3 µm. Other perovskites with optoelectronic applications like $CH_3NH_3PbI_3$,[23] $CH_3NH_3PbBr_3$,[23b] and $CsPbI_3$ microwires[24] have also been found to follow Jonscher's conductivity power law. Interestingly, the separation between two frequency ranges with different s has also been reported previously,[23a] but in $CH_3NH_3PbI_3$.

From the photoconductivity in Figure 6a, note first that σ seems to increase around 10 times similarly along the entire region of the spectra, which suggests a strong ionic-electronic connection. This could also agree with the low s value for σ_e, below more typical 0.8–1.0 reports.[17–19] Second, with light the characteristic ionic activation frequency f_i shifts approximately from 10 to 100 Hz, as indicated by the empty dots. In the polarization experiment presented in Figure S3c (Supporting Information), further artifacts are also found, due to the ion migration.

The high photoconductive gain and good electrical properties already suggest a possible application as a photodetector. We therefore recorded the responsivity of the device in the range of 384–650 nm. A bias of 2 V was applied to the lateral ITO finger contacts with a pitch of 20 µm resulting in an electric

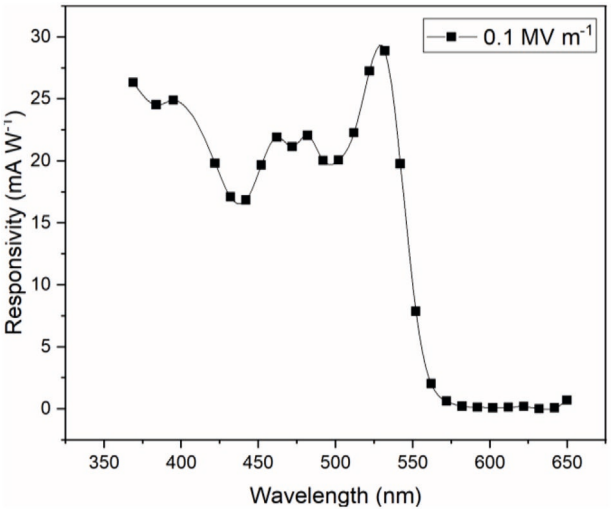

Figure 7. Responsivity of the AD films in the range of 384–650 nm. The bias is set to 0.1 MV m^{-1}.

field of 0.1 MV m^{-1}. We denote that such fields are exceptional low for photodetector operations. Such low fields were chosen in order to keep the impact of pure photoconductive effects as small as possible. A high wavelength dependent responsivity between 17 and 57 mA W^{-1} is recorded which quickly drops to zero for wavelengths above the bandgap (**Figure 7**). Biasing the sample with an electric field twice as strong results to responsivity values almost 4 times higher, indicating a nonlinear influence of field induced carrier injection on top of effects (Figure S4, Supporting Information). Otherwise, the shape of the responsivity curve is not affected by changing the bias voltage. Additionally, we want to point out the remarkable stability of these films. The samples were characterized over a period of 6 months (unpackaged, stored in air) after fabrication and still do not show any signs of degradation.

3. Conclusion

In summary, we showed that aerosol deposition is a viable method to produce low-cost, scalable semiconducting $CsPbBr_3$ films at room temperature with a quality which is already compatible for simple low-end optoelectronic applications. We found that perovskites can form compact layers with good adhesive properties on interdigitated ITO electrodes. Structural investigations showed that the crystal structure is only negligibly altered by the strenuous AD process. PL spectra and corresponding numerical models revealed that defects are generated, especially upon the impact on the hard substrate. Hereby, the defect density of the bottom layer right next to the substrate is about 10 times higher than the defect density in the top layer regime. Nevertheless, electrical characterizations confirmed that the good semiconducting properties of $CsPbBr_3$ are retained and reveal significant photoconductivity for both fast electronic and slow ionic transport. The combination of highly flexible deposition possibilities, high responsivity values, good electrical transport properties, and high stability advocate for applications as innovative photodetectors with geometries that were not feasible before.

Table 2. $CsPbBr_3$ film deposition parameters.

Deposition feature	Property
Average starting particle size	≈1 µm
Substrate material	ITO finger electrode glass substrate
Substrate thickness	1 mm
Carrier gas	N_2
Number of scans	20
Velocity of scan	1 mm s^{-1}
Nozzle to substrate distance	5 mm
Size of the nozzle orifice	10×0.5 mm^2
Pressure in the deposition chamber	≈5 mbar
Carrier gas flow rate	2.0 L min^{-1}
Deposition area	20×10 mm^2
Film thickness	20–35 µm

4. Experimental Section

Sample Fabrication: Microcrystalline $CsPbBr_3$ powder was synthesized by mixing equimolar mixtures of CsBr (99.999% trace metal basis, Sigma-Aldrich) and $PbBr_2$ (99.999% trace metal basis, Sigma-Aldrich) in a solution process, as described by Stoumpos et al.[6] Particles with diameters in the range of hundreds of nm to 10 µm were synthesized (Figure S1, Supporting Information). $CsPbBr_3$ films with a thickness ≈20–35 µm were fabricated on glass substrates with ITO interdigitated electrodes (OSRAM Licht AG) using the AD process. Solution-processed $CsPbBr_3$ powder was ground with a mortar and pestle before sieving with a 100 µm mesh to remove large agglomerated particles. The powder was kept in a vacuum oven at 110 °C for 2 h for drying. The micrometer-sized powder was used to deposit on the substrate using N_2 as the carrier gas. The film fabrication parameters are listed in **Table 2**.

Structural Characterization: The crystal structure of the as-processed powder and the AD processed film were investigated using a powder X-ray diffractometer with Cu K_α (λ = 1.5406 Å) radiation under an acceleration condition of 40 kV and 25 mA (Bruker D8 Advance eco, Karlsruhe, Germany) in Bragg–Brentano geometry. Full pattern structural refinements were performed by using the program TOPAS Version 5.[25] The visual of the crystal structure was generated using VESTA 3.[26]

A Jeol JSM-7610F Schottky field emission scanning electron microscope (Japan) at 2 kV acceleration voltage was used to obtain high-resolution images of the samples.

Optical Characterization: Photoluminescence spectra were obtained with a PicoQuant FluoTime 300 fluorescence spectrometer at room temperature. A diode laser emitting 402.2 nm pulses with a repetition rate of 5 MHz and a FWHM of 50 ps was employed as the excitation source. The pulse energy was set between 0.16 and 42.5 pJ per pulse with a spot size of ≈26×10^3 µm². The radiation was resolved by a monochromator and detected by a PMA-C 192-N-M photomultiplier tube. All decay dynamics were recorded in time-correlated single photon counting (TCSPC) mode.

Absorbance spectra were measured with a Perkin-Elmer 950 spectrometer employing a 150 mm integrating sphere with a central mount holder. The samples were illuminated by a tungsten halogen lamp and the radiation was detected with a R6872 photomultiplier.

Electrical Characterization: The DC mode current–voltage ($I - V$) characteristics and the AC mode IS measurements were carried out in a grounded Faraday cage with a Zahner Zennium Pro potentiostat at room temperature and air condition. The sample was illuminated with a 405 nm peak blue light-emitting diode for light measurements. For the $I - V$ measurements, the scan rate was 100 mV s^{-1} and for the IS the *AC* perturbation amplitude was 150 mV.

For responsivity measurements, the tuneable LED light source TLS03 was connected to the potentiostat. The wavelength was set with a linear monochromator and the light intensity varied between 56 and 248 W m^{-2} depending on the selected wavelength. The light was sinusoidally modulated with a frequency of 300 Hz and integrated over 100 cycles to account for the dark current and measure the incident photon conversion efficiency. An image of the setup is depicted in Figure S5 (Supporting Information).

Supporting Information

Supporting Information is available from the Wiley Online Library or from the author.

Acknowledgements

O.A. acknowledges the financial support from the VDI/VD Innovation + Technik GmbH (Project-title: PV-ZUM). A.T and O.A. gratefully acknowledge the funding of the Erlangen Graduate School in Advanced Optical Technologies (SAOT) by the Bavarian State Ministry for Science and Art. N.H.K., U.E., K.G.W., and C.J.B. gratefully acknowledge financial support from the Deutsche Forschungsgemeinschaft (DFG) under MA 6617/1-1, IGK2495/E and IGK2495/F.

Conflict of Interest

The authors declare no conflict of interest.

Keywords

aerosol deposition, hysteresis, impedance spectroscopy, inorganic perovskites, photoluminescence spectroscopy

Received: November 27, 2020
Revised: December 16, 2020
Published online: January 15, 2021

[1] a) D. Hanft, J. Exner, M. Schubert, T. Stöcker, P. Fuierer, R. Moos, *Ceram. Sci. Technol.* **2015**, *06*, 147; b) G.-T. Hwang, V. Annapureddy, J. H. Han, D. J. Joe, C. Baek, D. Y. Park, D. H. Kim, J. H. Park, C. K. Jeong, K.-I. Park, J.-J. Choi, D. K. Kim, J. Ryu, K. J. Lee, *Adv. Energy Mater.* **2016**, *6*, 1600237; c) V. Annapureddy, Y. Kim, G.-T. Hwang, H. W. Jang, S.-D. Kim, J.-J. Choi, B. Cho, J. Ryu, *Adv. Mater. Interfaces* **2018**, *5*, 1700811; d) J. Akedo, M. Lebedev, *Appl. Phys. Lett.* **2000**, *77*, 1710; e) C.-W. Ahn, J.-J. Choi, J. Ryu, B.-D. Hahn, J.-W. Kim, W.-H. Yoon, J.-H. Choi, D.-S. Park, *Carbon* **2015**, *82*, 135; f) M. Iwanami, M. Nakada, H. Tsuda, K. Ohashi, J. Akedo, *IEICE Electron. Express* **2007**, *4*, 26; g) J.-J. Choi, J. Ryu, B.-D. Hahn, C.-W. Ahn, J.-W. Kim, W.-H. Yoon, D.-S. Park, *Int. J. Hydrogen Energy* **2014**, *39*, 12878; h) E.-S. Kim, J.-G. Liang, C. Wang, M.-Y. Cho, J.-M. Oh, N.-Y. Kim, *Sci. Rep.* **2019**, *9*, 680;. i) C. Lee, M.-Y. Cho, M. Kim, J. Jang, Y. Oh, K. Oh, S. Kim, B. Park, B. Kim, S.-M. Koo, J.-M. Oh, D. Lee, *Sci. Rep.* **2019**, *9*, 2166.

[2] a) S. H. Cho, Y. J. Yoon, *Thin Solid Films* **2013**, *547*, 91; b) S. Yang, H. Kim, S.-H. Ahn, C. S. Lee, *Electrochim. Acta* **2015**, *166*, 117; c) S. Hirose, Y. Ezuka, J. Akedo, S. Kunugi, S. Yoguchi, S. Nakajima, (National Institute of Advanced Industrial Science and Technology, Tokyo (JP); Sekisui Chemical Co. Ltd.,Osaka (JP)) *Patent US 9721733 B1*, **2017**.

[3] F. Panzer, D. Hanft, T. P. Gujar, F.-J. Kahle, M. Thelakkat, A. Köhler, R. Moos, *Materials* **2016**, *9*, 277.

[4] a) M. Y. Cho, S. Kim, I. S. Kim, E. S. Kim, Z. J. Wang, N. Y. Kim, S. W. Kim, J. M. Oh, *Adv. Funct. Mater.* **2020**, *30*, 1907449; b) S. Kim, M. Y. Cho, I. S. Kim, W. J. Kim, S. H. Park, S. Baek, J. M. Oh, S. W. Kim, *Adv. Mater. Interfaces* **2019**, *6*, 1900359.

[5] J. Akedo, *J. Therm. Spray Technol.* **2008**, *17*, 181.

[6] C. C. Stoumpos, C. D. Malliakas, J. A. Peters, Z. Liu, M. Sebastian, J. Im, T. C. Chasapis, A. C. Wibowo, D. Y. Chung, A. J. Freeman, B. W. Wessels, M. G. Kanatzidis, *Cryst. Growth Des.* **2013**, *13*, 2722.

[7] a) N. H. Khansur, U. Eckstein, K. Riess, A. Martin, J. Drnec, U. Deisinger, K. G. Webber, *Scr. Mater.* **2018**, *157*, 86; b) J. Adamczyk, P. Fuierer, *Surf. Coat. Technol.* **2018**, *350*, 542; c) N. H. Khansur, U. Eckstein, L. Benker, U. Deisinger, B. Merle, K. G. Webber, *Ceram. Int.* **2018**, *44*, 16295.

[8] Y. Rakita, S. R. Cohen, N. K. Kedem, G. Hodes, D. Cahen, *MRS Commun.* **2015**, *5*, 623.

[9] A. C. Dent, C. R. Bowen, R. Stevens, M. G. Cain, M. Stewart, *J. Eur. Ceram. Soc.* **2007**, *27*, 3739.

[10] a) M. Sebastian, J. A. Peters, C. C. Stoumpos, J. Im, S. S. Kostina, Z. Liu, M. G. Kanatzidis, A. J. Freeman, B. W. Wessels, *Phys. Rev. B* **2015**, *92*, 235210; b) G. J. Matt, I. Levchuk, J. Knüttel, J. Dallmann, A. Osvet, M. Sytnyk, X. Tang, J. Elia, R. Hock, W. Heiss, C. J. Brabec, *Adv. Mater. Interfaces* **2020**, *7*, 1901575.

[11] H. Shi, M.-H. Du, *Phys. Rev. B* **2014**, *90*, 174103.

[12] J. Chen, D. J. Morrow, Y. Fu, W. Zheng, Y. Zhao, L. Dang, M. J. Stolt, D. D. Kohler, X. Wang, K. J. Czech, M. P. Hautzinger, S. Shen, L. Guo, A. Pan, J. C. Wright, S. Jin, *J. Am. Chem. Soc.* **2017**, *139*, 13525.

[13] J. Song, Q. Cui, J. Li, J. Xu, Y. Wang, L. Xu, J. Xue, Y. Dong, T. Tian, H. Sun, H. Zeng, *Adv. Opt. Mater.* **2017**, *5*, 1700157.

[14] Y. Wang, Y. Ren, S. Zhang, J. Wu, J. Song, X. Li, J. Xu, C. H. Sow, H. Zeng, H. Sun, *Commun. Phys.* **2018**, *1*, 96.

[15] P. Lopez-Varo, J. A. Jiménez-Tejada, M. García-Rosell, S. Ravishankar, G. Garcia-Belmonte, J. Bisquert, O. Almora, *Adv. Energy Mater.* **2018**, *8*, 1702772.

[16] a) O. Almora, G. Garcia-Belmonte, *Sol. Energy* **2019**, *189*, 103; b) O. Almora, C. Aranda, G. Garcia-Belmonte, *J. Phys. Chem. C* **2018**, *122*, 13450.

[17] A. K. Jonscher, *Nature* **1977**, *267*, 673.

[18] a) J. C. Dyre, T. B. Schrøder, *Rev. Mod. Phys.* **2000**, *72*, 873; b) S. R. Elliott, *Solid State Ionics* **1994**, *70–71*, 27; c) J. C. Dyre, P. Maass, B. Roling, D. L. Sidebottom, *Rep. Prog. Phys.* **2009**, *72*, 046501.

[19] a) M. Pollak, G. E. Pike, *Phys. Rev. Lett.* **1972**, *28*, 1449; b) W. K. Lee, J. F. Liu, A. S. Nowick, *Phys. Rev. Lett.* **1991**, *67*, 1559;. c) L. Murawski, R. J. Barczyński, D. Samatowicz, *Solid State Ionics* **2003**, *157*, 293; d) A. Mansingh, *Bull. Mater. Sci.* **1980**, *2*, 325.

[20] S. R. Elliott, A. P. Owens, *Philos. Mag. B* **1989**, *60*, 777.

[21] a) G. Conte, F. Somma, M. Nikl, *Phys. Status Solidi C* **2005**, *2*, 306; b) G. Vitale, G. Conte, P. Aloe, F. Somma, *Mater. Sci. Eng., C* **2005**, *25*, 766.

[22] P. Maji, A. Ray, P. Sadhukhan, S. Chatterjee, S. Das, *J. Appl. Phys.* **2018**, *124*, 124102.

[23] a) M. S. Sheikh, A. P. Sakhya, A. Dutta, T. P. Sinha, *Thin Solid Films* **2017**, *638*, 277; b) M. S. Sheikh, A. P. Sakhya, P. Sadhukhan, A. Dutta, S. Das, T. P. Sinha, *Ferroelectrics* **2017**, *514*, 146.

[24] P. Maji, S. Chatterjee, S. Das, *Ceram. Int.* **2019**, *45*, 6012.

[25] A. Bruker, *User's Manual, Bruker AXS*, Karlsruhe, Germany **2014**.

[26] K. Momma, F. Izumi, *J. Appl. Crystallogr.* **2011**, *44*, 1272.